City Research Online

City, University of London Institutional Repository

City Research Online: http://openaccess.city.ac.uk/   publications@city.ac.uk

Upstream Shear Layer Stabilisation via Self-Oscillating Trailing Edge Flaplets

Edward Talboys [*][1] and Christoph Brücker[1]

[1]*City, University of London, Northampton Square, London, EC1V 0HB*

Abstract

The flow around a symmetric aerofoil (NACA 0012) with an array of flexible flaplets attached to the trailing edge has been investigated at Reynolds numbers of 100,000 - 150,000 by using time resolved particle image velocimetry (TR-PIV) and high speed motion tracking of the flaplets' tips. Particular attention has been made on the upstream effect on the boundary layer evolution along the suction side of the wing. For the plain aerofoil, without flaplets, the boundary layer on the second half of the wing undergoes shear-layer roll-up in the fundamental mode, but with rapid growth of non-linear modes which initiate the merging of rollers. When the flaplets are attached, it is shown that the flow-induced oscillations of the flaplets are able to create a lock-on effect that stabilises the linear state of the shear layer whilst damping the growth of non-linear modes. In addition, it is concluded that the modified trailing edge reduces aeroacoustic noise production in the lower frequency band, as indicated by an initial acoustic investigation.

1   Introduction

The main source of aerodynamic tonal noise generated on aerofoils is due to the trailing edge turbulent boundary layer interaction. And as such this noise signature plays a crucial role in practically all aerodynamic applications; from aircraft to wind turbines and ventilation systems. To mitigate this aeroacoustic interaction many possible approaches exist, among them are serrated edges, slitted trailing edges, brush-like edge extensions or porous materials. In the present study, a flexible trailing edge consisting of an array of small elastic flaplets, mimicking the tips of bird feathers, is used. The specific arrangement and structure of feathers on the trailing edge of an owl's wing is well known to be one of the key mechanisms that the bird used to enhance noise suppression (Jaworski and Peake, 2013). In addition, secondary feathers on the upper side of the wings of the steppe eagle (*Aquila nipalensis*) (Carruthers et al., 2007) and the peregrine falcon (*Falco peregrinus*) (Ponitz et al., 2014), to give a few examples, have been observed to pop-up as the birds attack prey or come into land at a high angle of attack. This phenomena has been the subject of many research studies. Schlüter (2010) could show that by attaching rigid flaps, via a hinge, on the upper surface of the wing, the

Symbol	Units	Description
U_∞	m/s	Free-stream velocity
U_0	m/s	Convective velocity
U_{es}	m/s	Boundary layer edge velocity
u'	m/s	Streamwise velocity fluctuations
v'	m/s	Wall normal velocity fluctuations
Re_c	—	Chord based Reynolds Number
α	o	Angle of attack
f_0	Hz	Shear layer fundamental frequency
$f_{0-1/2}$	Hz	Shear layer instability frequency
f_k	Hz	Vibration frequency at k^{th} mode
α_k	—	Wave-number at the kth vibration mode
λ_0	m	Shear layer roll-up wavelength
St_0^*	—	Shear layer Strouhal Number
s	m	Spanwise width of flaplet
L	m	Length of flaplet
d	m	Spacing between flaplet
T	m	Thickness of flaplet
w	m	Flaplet vertical displacement
ζ	—	Damping coefficient
ω_n	rad/s	Natural Frequency
ω_d	rad/s	Damped Frequency
E	N/m^2	Elastic Modulus
I	m^4	Area moment of inertia
ρ	kg/m^3	Density

Table 1: Nomenclature Table

C_L max is increased for a series of tested aerofoils (NACA 0012, NACA 4412, SD 8020). Schlüter also showed that the flaps bring the additional benefit of gradual stall rather than a more severe lift crisis. Osterberg and Albertani (2017) carried out a similar study on a flat plate subjected to high angles of attack, coming to the same conclusion. Brücker and Weidner (2014) used flexible flaplets attached on the suction side of a NACA 0020 aerofoil that was subjected to a ramp-up motion. The results show a considerable delay in dynamic stall. Flap length and flap chordwise spacing were varied and it was found that the most successful configuration was two rows of flaps of length 0.1c spaced 0.15c-0.2c in the chordwise direction. The wavelength of the rollers in the shear layer was found to be of the same order, 0.15c-0.2c. This led to the conclusion that the flaplets resulted in a lock-in effect with these rollers, as the two spacing length scales were comparable. Concluding that this lock-in effect stabilizes the shear layer. Rosti et al. (2017) then built on

arXiv:1804.07520v2 [physics.flu-dyn] 26 Apr 2018
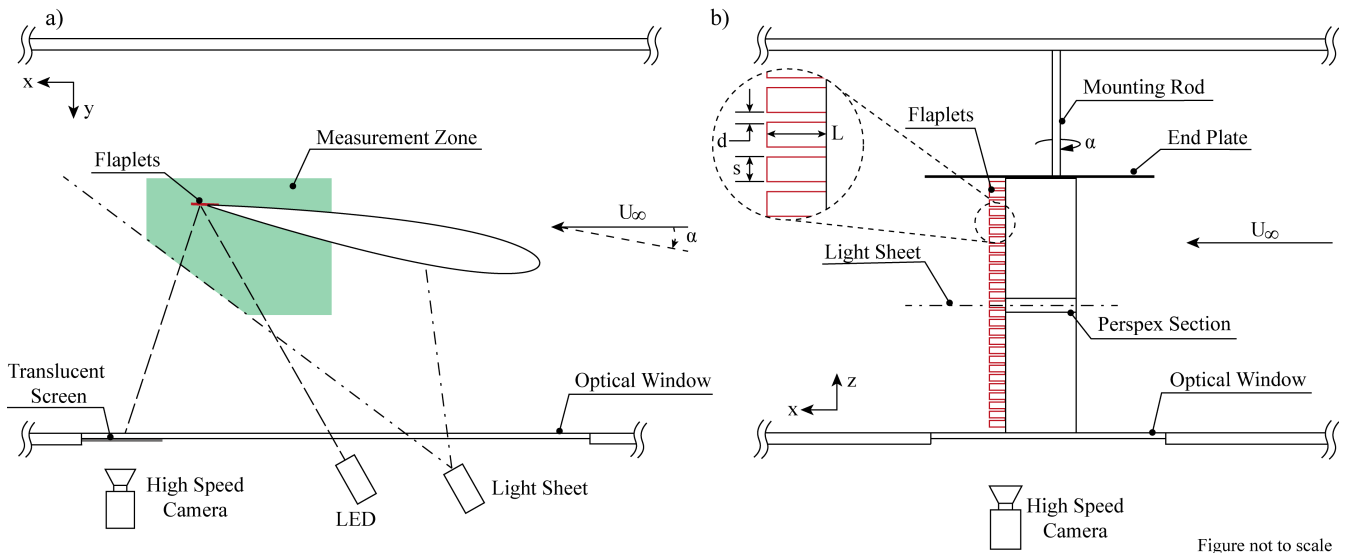
Figure 1: a) Plan view of the experimental set-up. b) Side view of the experimental set-up

these findings of by carrying out a DNS (direct numerical simulation) parametric study. The flap element was rigid but coupled to the aerofoil surface by a torsional spring type coupling. It was found that when the flap oscillations were at the same frequency as the shear-layer roll up, the mean lift coefficient was at it's highest.

Similar effects, as observed for aerofoils, could also be seen on tests with bluff bodies. A series of studies on cylinder flows with flaplets attached on the aft half of the cylinder have been carried out by Kunze and Brücker (2012); Kamps et al. (2016); Geyer et al. (2017). Kunze and Brücker (2012) saw that the presence of the flexible elements allowed the shedding frequency to be locked in with the most dominant eigen-frequency of the flaplets. This hints to a similar lock-in effect of the shear layer roll-up observed for the aerofoils, Rosti et al. (2017). Consequently the flow-structure in the wake is changed and a reduced wake deficit is observed. Kamps et al. (2016) then tested the same cylinder/flaplet configuration in an aeroacoustic wind tunnel and could show that the flaplets overall reduce noise, both in the tonal and the broadband components.

The present study builds off these previous studies in order to study the benefit/impact of flexible flaplets being attached to the trailing edge rather than on the aerofoil body. Initial tests of such modifications of the trailing edge by Kamps et al. (2017) already showed promising results in noise reduction. However, no details of the flow structure and the fluid-structure interaction is known which might explain the observed aeroacoustical modification. This is the purpose of the present study.

2 Experimental Set-Up

The experiments were carried out in the Handley Page laboratory at City, University of London in a closed loop wind tunnel. The test section of the tunnel is 0.81m and 1.22m in cross-section, and has a turbulence intensity of 0.8%. A NACA 0012 aerofoil, with a chord of 0.2m and span of 0.52m, was used for the present study. One side of

the aerofoil spanned to the floor of the tunnel and an endplate was affixed to the exposed end to negate any end effects. The aerofoil was 3D printed in two sections with a small perspex section in the measurement window, as per figure 1b. The use of perspex in this region improves the quality of the PIV recordings close to the surface. Three chord based Reynolds numbers were analysed in this study, 100,000, 125,000 and 150,000, at two different angles of attack, 0° and 10°. A 0.3 mm thick boundary layer trip was implemented at 0.2c on both sides of the aerofoil to ensure that the boundary layer was turbulent.

The trailing edge with the flexible flaplets was made from a polyester foil, of thickness 180μm, which was laser-cut at one long side to form an array of individual uniform flaplets. Each flaplets has a length of L = 20mm, a width of s = 5mm and an interspacing of d = 1mm in spanwise direction (see 1b). The foil was adhered to the pressure side of the aerofoil using thin double sided tape such that the flaplets face downstream, with their free end located at a distance of x/c = 1.1c downstream of the trailing edge. The flaplets form a mechanical system whereby each flaplet is a rectangular cantilever beam which is free to oscillate perpendicular to the mean-flow direction.

2.1 Velocity Field Measurements

Time Resolved Particle Image Velocimetry (TR-PIV) measurements were carried out using a 2mm thick double pulsed Nd:YLF laser sheet in a standard planar set-up. A high speed camera (Phantom Miro M310, window size 1280 x 800 pixels) equipped with a macro lens, Tokina 100mm, with f/8 was used in frame straddling mode. Olive oil seeding particles, of approximate size 1μm, were added to the flow downstream of the model. 500 pairs of images were obtained at a frequency of 1500 Hz with the pulse separation time being altered for each case, given in Table 2.

The raw images were then processed using the TSI Insight 4G software which uses the method of 2D cross correlation. The first pass interrogation window size was 32 x 32 pixels,

Re$_c$	Aperture Size	Pulse Separation	Capture Frequency
100,000	f/8	80 μs	1500 Hz
150,000	f/8	30 μs	1500 Hz

Table 2: TR-PIV parameters used for the two different Re$_c$

Test Name	Re$_c$	α	Trailing Edge
100-0-P	100,000	0	Plain
100-0-F	100,000	0	Flaplets
100-10-P	100,000	10	Plain
100-10-F	100,000	10	Flaplets
150-0-P	150,000	0	Plain
150-0-F	150,000	0	Flaplets
150-10-P	150,000	10	Plain
150-10-F	150,000	10	Flaplets

Table 3: Test matrix nomenclature

with a 50% overlap. The size was then reduced to 16 x 16 pixels for the subsequent pass. A 3 x 3 median filter was then applied to validate the local vectors, any missing or spurious vectors were interpolated by using the local mean.

2.2 Flap Motion Tracking

To track and record the real time motion of the flaplets with high resolution, a high power LED (HARDsoft IL-106G) was used alongside a second high speed camera (Phantom Miro M310) with a Nikon 50mm f/1.8 lens. The LED was directed at the flaplets and the back reflections were seen on a translucent screen adhered to the transparent wind tunnel side wall (see figure 1a). Due to the optical lever-arm condition, small deflections of the flaplets lead to a large displacement of the back-scattered light on the screen. The recordings were taken at 3200 Hz, with an exposure time of 320μs and an aperture of f/1.8. In total 2.5 seconds of motion was recorded on the Phantom Camera Control Application (PCC), resulting in 8000 images for each case. An edge detection code (Matlab) was then used to track and record the flap tips motion over time. Spurious data points were removed from the data set and subsequently interpolated prior to a low pass filter being applied to the data.

3 Results

The test cases mentioned in section 2, were run both with and without the flaplets in order to ascertain a baseline for comparative analysis. For the remainder of the report the nomenclature in Table 3 will be used and only results for Re$_c$=100,000 and Re$_c$=150,000 are shown.

3.1 Flaplet Dynamics

As previously mentioned (sect. 2.2), the flaplets can be understood as thin cantilever beams, clamped at one side and free to oscillate at the tip in a viscous environment. The subsequent equation of motion follows from bending beam

Property	Value
f_1 at α_1	107 Hz
f_2 at α_2	671 Hz
ρ_{flap}	1440 kg/m^3
E$_{\text{flap}}$	3.12 GPa

Table 4: Flaplet dynamics and material properties

theory and leads to the following ODE (Stanek, 1965).:

$$EI\frac{\partial^2 w}{\partial x^4} = -\rho A\frac{\partial^2 w}{\partial t^2} - \frac{c}{L}\frac{\partial w}{\partial t} \tag{1}$$

The general solution for an under-damped harmonic oscillators is then as followed:

$$\hat{w}(t) = \frac{w}{w_0}e^{-\zeta \omega_n t}cos(\omega_d t - \phi) \tag{2}$$

To find the natural frequencies at which vibration mode is activated, the boundary condition of no viscous damping is applied on the system. And from equation 1, equation 3 is then obtained:

$$f_k = \frac{\alpha_k^2 T}{2\pi L^2}\sqrt{\frac{EI}{12\cdot\rho}} \tag{3}$$

A step-response test was conducted with a single flaplet being bent out of the equilibrium position and subsequently released from a set vertical height, w_0, allowing the flaplet to oscillate back to its equilibria. The tip motion was then recorded by a high speed camera (Phamtom Miro M310, 1200 x 800px at 3200Hz). The previously mentioned edge detection script was used to track the tip of the flaplet. The recorded response, figure 2, indeed resembles that of a weakly damped harmonic oscillator. The natural frequency of the flaplets is 107Hz as obtained by analysing the response via fast fourier transform (FFT). With the known solution of equation 3, for the weakly damped harmonic oscillator, and by using the first Eigen mode, $\alpha_1 = 1.875$, one can estimate the Young's Modulus of the material used. Equation 3 has been further used to evaluate at which point the flaplets will go into their second vibration mode, for this case $\alpha_2 = 4.694$ leading to $f_2 = 671$ Hz.

3.2 Flow Field

A virtual velocity probe was placed in the measured velocity field at a suitable location ($x/c = 0.85$ and $y/c = 0.05$) in the boundary layer to detect instabilities. This was done by means of evaluating the fluctuating vertical component (v') time-series at the probe location. A peak in the v' velocity corresponds to the presence of a shear layer roll-up vortex passing through the probe area as revealed by the TR-PIV results. Therefore the time history of this probe was analysed and the frames corresponding to a peak in the v' velocity component were conditionally averaged. To recover the transportation of these coherent structures, the frames preceding and following the 'peak' frames were also averaged. From these averaged frames the Q-criterion was computed, see figure 3. Temporal evolution of the vortex
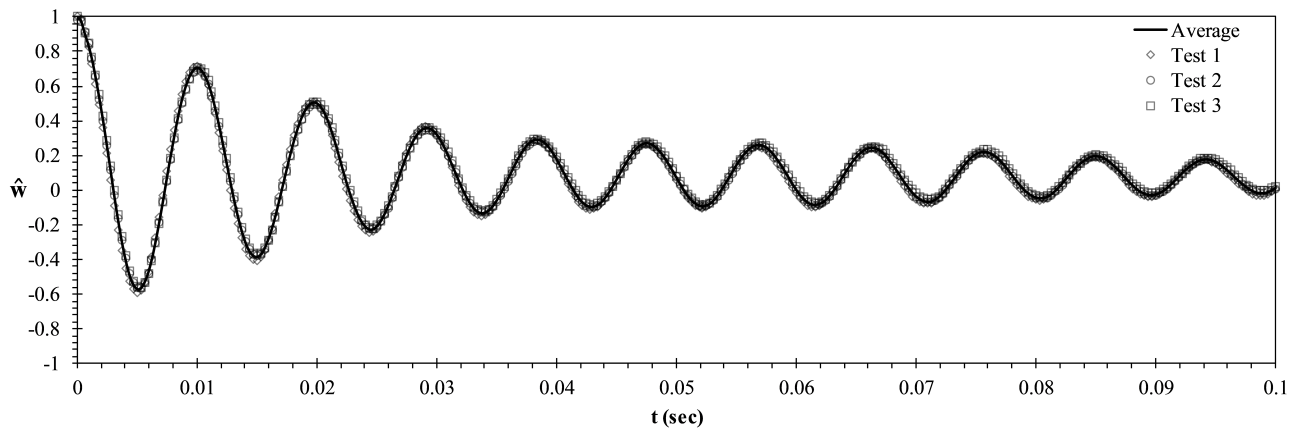
Figure 2: Response of a singular flaplet to a step input.

cores position, allows the convection speed to be calculated. All cases fall in the range U_0/U_∞ = 0.5 - 0.55. A further breakdown of the individual cases can be seen in table 6.

A proper orthogonal decomposition (POD) of the fluctuating velocity field was carried out and this is utilised to aid understanding of the spectral results. Each of the POD modes are associated with the most dominant features in the flow. In the present case the dominate features are the observed shear layer vortices as seen in figure 3.

It is well understood that the eigenvectors of each POD mode gives the temporal signature of the mode (Semeraro et al., 2012; Meyer et al., 2007). Therefore performing a spectral analysis on the eigenvectors yields the frequency of structure observed in the mode. From the spectral analysis of the $4^{th} v'$ mode, figure 4a, it is seen that this mode corresponds to the fundamental shear layer instability mode. In comparison, the 2nd mode, figure 4b, shows half of the fundamental frequency ($f_{0-1/2}$). This mode indicates the presence of a non-linear state in the shear-layer which is the observed pairing of successive rollers, explaining the factor two reduction in frequency. POD also gives a graphical representation of the dominant structures and as such the wavelength of the fundamental shear-layer mode can be estimated.

When analysing the velocity probe data for the zero degree cases, it was seen that no obvious spectral peaks were present. The shear layer at these conditions is expected to be in the sub-critical state as the adverse pressure gradient is weaker compared to the 10° angle of attack situation. (Huang and Lin, 1995).

Table 5, shows the compiled results of Figure 5 and the results of the Reynolds 100,000 cases. The theoretical case is from the empirical equation proposed by Tam (1974) for a NACA 0012 at 10° angle of attack (equation 4).

$$f_0 = 11.8 \, n \, U_\infty^{0.8} \tag{4}$$

Where n is a integer related to the velocity, for the present case has been selected to be unity. It must be noted that the free stream velocity is in imperial units (ft/sec), thus must be converted to obtain the correct correlation. The empirical results show good agreement with those found by the PIV results, giving further confidence in the results. However Chong et al. (2013) advised caution with Tam's

Test Cases	PIV Probe		POD	
	f_0	$f_{0-1/2}$	f_0	$f_{0-1/2}$
100-10-P	150 Hz	—	150 Hz	—
100-10-F	132 Hz	—	132 Hz	—
Theory	160 Hz	—	—	—
150-10-P	234 Hz	156 Hz	234 Hz	144 Hz
150-10-F	246 Hz	114 Hz	246 Hz	114 Hz
Theory	221 Hz	—	—	—

Table 5: Shear layer fundamental and non-linear instability frequencies detected by the PIV probe and POD modes from figure 5, with a theoretical result (Tam, 1974) for comparison.

proposed model as it seemingly deviated from experimental results at higher frequencies. Further agreement is found with experimental trends from Huang and Lin (1995) who graphically present a frequency of ∼100Hz - 200Hz, for the tabulated cases.

When observing the 150-10-P spectra result from the velocity probe, figure 5a, it is seen that the strongest peak is at ∼ $f_{0-1/2}$ position. This is indicating that the non-linear state is already dominating with rows of large, merged vortices present in the flow. These vortices will carry an increased lower tonal noise signature and therefore are undesirable. This merging effect has been seen in many previous planar shear flow literatures (Ho and Huang, 1982; Rajagopalan and Antonia, 2005; Rodríguez et al., 2013; Perret, 2009). It must be noted here that this dominant frequency is not truly half, and is thought to be because the position of the transition point of the instability is randomly fluctuating in the shear layer; hence giving a more 'broadband' region where this frequency is seen (Prasad and Williamson, 1997; Rajagopalan and Antonia, 2005; Dong et al., 2006; Yarusevych et al., 2009). Once the flaplets are attached to the aerofoil, figure 5b, the $f_{0-1/2}$ frequency is suppressed and the f_0 is now the dominant frequency. This indicates that the shear-layer is stabilized and the growth of non-linear modes is reduced, thus reducing the tendency of vortex pairing. This stabilization is thought to be caused by a lock-on effect between the oscillating flaplets and the
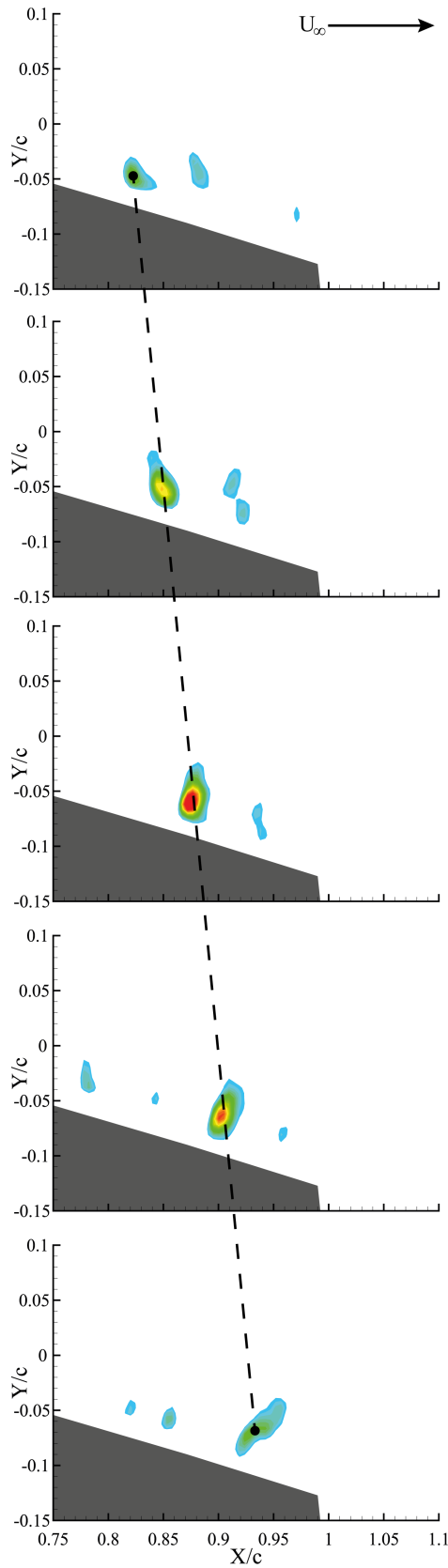
Figure 3: Q-Criterion for case 100-10-F. Time spacing in between each image is: $\Delta t^* = \Delta t \cdot U_\infty/c = 0.055$
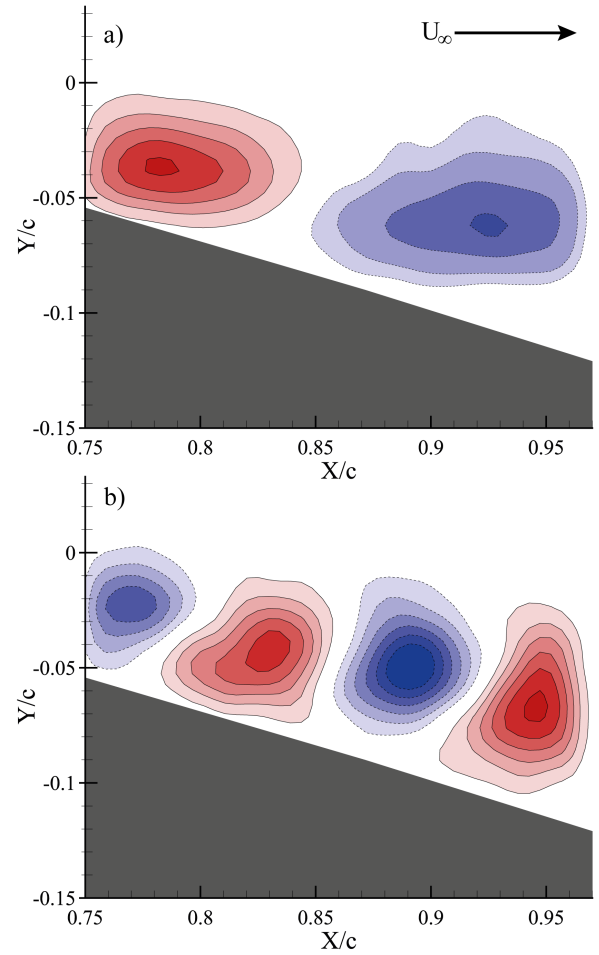

Figure 4: v' POD mode comparison for the case 150-10-F. a) Mode 2, corresponding to $f_{0-1/2}$ b) Mode 4, corresponding to f_0

fundamental shear-layer instability, a similar effect to that presented by Kunze and Brücker (2012).

Yarusevych et al. (2009), proposed that the Strouhal number for shear layer flows should be scaled with the wavelength of the fundamental shedding, and the boundary layer edge velocity rather than the previously suggested momentum thickness. Analytically Yarusevych et al. (2009) showed that this quantity should be in the region of 0.45 $\leq$ St$_0^*$ $\leq$ 0.5. Results in table 6, shows that in the present case the values obtained for St$_0^*$ are in the region of the suggested values. The values of λ_0 were obtained from the POD analysis (figure 4). Similar wavelengths were observed by Brücker and Weidner (2014), where the wavelength they

Test Case	f_0	U_0/U_∞	λ_0	U_{es}/U_∞	St$_0^*$
100-10-P	150 Hz	0.524	0.138c	1.02	0.514
100-10-F	132 Hz	0.518	0.154c	1.02	0.505
150-10-P	234 Hz	0.547	0.125c	1.04	0.472
150-10-F	246 Hz	0.544	0.131c	1.04	0.523

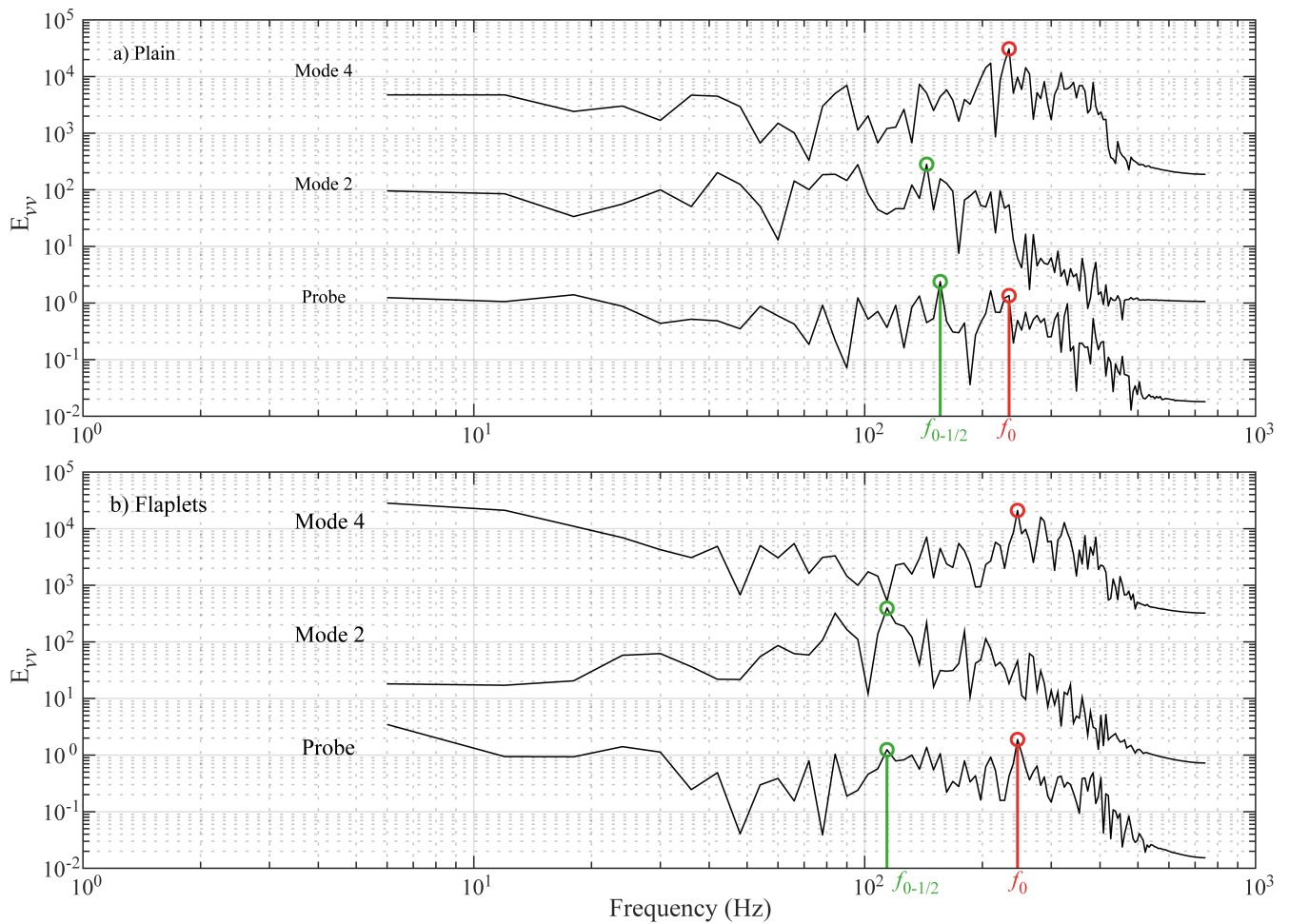Table 6: Fundamental frequency Strouhal number comparison

Figure 5: Spectral analysis of the v' (probe), $4^{\text{th}} v'$ POD mode and $2^{\text{nd}} v'$ POD mode. Each spectra is spaced by two decades for clarity.

found was 0.15c - 0.2c.

For the lowest Reynolds Number cases (100-10-P & 100-10-F), there was no dominating shear layer instabilities/pairing (i.e. $f_{0-1/2}$) observed in the spectral analysis. And as such the flaplets had no observable effect on the flow field. The reason for this is thought to be because of the sub-critical state of the shear-layer formation at the lower flow speed (Prasad and Williamson, 1997; Rajagopalan and Antonia, 2005).

3.3 Flaplet Motion

For the motion study, three neighbouring flaplets were analysed in order to distinguish between random motion patterns, representing turbulent structures, or spanwise coherent structures such as the described rollers convecting along the flaplets. The flaplet motion has been classed into two different categories, synchronous in-phase (S) motion and anti-synchronous (A-S) motion. The S motion is when all three flaplets are in the same phase, both for positive and negative deflections (see figure 6a for clarity). A-S motion is defined as when the flaplets have a phase delay of π with respect to each other (see figure 6b). The motion was recorded and analysed for 2.5 seconds leading to a total of 8000 frames. To investigate the probabilities of whether the flaplets have S or A-S motion the flaplet eigen frequency,
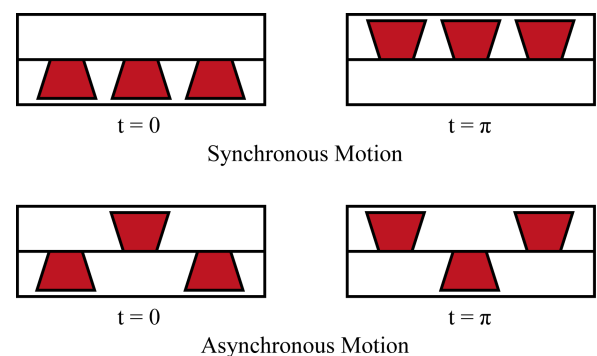

Figure 6: Sketch of the flaplets in either synchronous or asynchronous motion, looking from a downstream view of the trailing-edge.

f_1=107Hz, is used to calculate the maximum number of possible 'flap events' in the sampling time, which is 535 over the captured period.

Test Case	P(S)	P(A-S)
100-0-F	0.104	0.023
150-0-F	0.074	0.036
100-10-F	0.225	0.009
150-10-F	0.162	0.016

Table 7: Flaplet motion synchronisation probabilities

When observing the 10° cases in Table 7, it can be seen that the S motion has a significantly higher probability than the A-S motion. This is due to the strong spanwise coherence of the shear layer vortices. An interesting observation is that the 100-10-F case has a higher probability of S motion compared to 150-10-F. This is because for the first case the shear layer fundamental frequency, f_0, is closer to the Eigen frequency of the flaplets and therefore the lock-in effect is more pronounced. In comparison, for an angle of 0°, the flaplet motion is much more random. This is due to the weaker adverse pressure gradient on the upper side of wing, which reduces the mean shear in the inflection point of the boundary layer (BL). Thus, the motion of the flaplets here is thought to be mainly due to small scale turbulent structures convected downstream and exciting the flaplets.

4   Conclusion

Placing flexible flaplets on the trailing edge on an aerofoil at a moderated angle of attack (10°) has been seen to have a profound upstream effect on the boundary layer, leading to a stabilisation of the fundamental mode growing in the shear-layer on the suction side along the second half of the wing. Without the flaps, further growth of non-linear instabilities leads to pairing of the spanwise rollers near the trailing edge. This non-linear behavior is clearly suppressed by attaching the flaplets, and the effect is more pronounced when the frequency of the fundamental shear-layer mode is closer to the Eigen-frequency of the flaplets. This observation leads to the conclusion that the stabilisation is due to the lock-on of the flaplets oscillating with the fundamental instability mode. At zero angle of attack, the effect is not observed as the BL is not developed towards the critical state. A further consequence of the lock-on is speculated to be a reduction in the boundary layer thickness due to the reduced probability of the pairing events, which are responsible for the average increase in boundary layer thickness. This leads to a reduction in the wake deficit and thus a reduction in the aerofoil's drag. A previous study has also seen this effect on a cylinder with flaplets attached on the aft half (Kunze and Brücker, 2012). The in-phase oscillations of neighbourhing flaplets indicate the spanwise coherence of the rollers formed in the BL at an angle of 10 degrees, which dominates the excitation of the flaps compared to small-scale turbulences convected along the flaps. The present study supports preliminary aeroacoustic results which shows the beneficial effect of damping of low-frequency content of the generated noise by the flaplets (Kamps et al., 2017). A more definitive aeroacoustic conclusion and quantitative integral force measurements are left as future work.

5   Acknowledgements

References

Brücker C, Weidner C (2014) Influence of self-adaptive hairy flaps on the stall delay of an airfoil in ramp-up motion. J Fluids Struct 47:31–40, DOI 10.1016/j.jfluidstructs.2014.02.014

Carruthers AC, Thomas ALR, Taylor GK (2007) Automatic aeroelastic devices in the wings of a steppe eagle Aquila nipalensis. J Exp Biol 210(23):4136–4149, DOI 10.1242/jeb.011197

Chong TP, Joseph PF, Kingan MJ (2013) An investigation of airfoil tonal noise at different Reynolds numbers and angles of attack. Appl Acoust 74(1):38–48, DOI 10.1016/j.apacoust.2012.05.016

Dong S, Karniadakis GE, Ekmekci A, Rockwell D (2006) A combined direct numerical simulation-particle image velocimetry study of the turbulent near wake. J Fluid Mech 569:185–207, DOI 10.1017/S0022112006002606

Geyer TF, Kamps L, Sarradj E, Brücker C (2017) Passive Control of the Vortex Shedding Noise of a Cylinder at Low Reynolds Numbers Using Flexible Flaps. 23rd AIAA/CEAS Aeroacoustics Conf pp 1–11, DOI 10.2514/6.2017-3015

Ho CM, Huang LS (1982) Subharmonics and vortex merging in mixing layers. J Fluid Mech 119:443–473, DOI 10.1017/S0022112082001438

Huang R, Lin C (1995) Vortex shedding and shear-layer instability of a cantilever wing at low reynolds numbers. 33rd Aerosp Sci Meet Exhib 33(8):1398–1403, DOI 10.2514/3.12561

Jaworski JW, Peake N (2013) Aerodynamic noise from a poroelastic edge with implications for the silent flight of owls. J Fluid Mech 723:456–479, DOI 10.1017/jfm.2013.139

Kamps L, Geyer TF, Sarradj E, Brücker C (2016) Vortex shedding noise of a cylinder with hairy flaps. J Sound Vib 388:69–84, DOI 10.1016/j.jsv.2016.10.039

Kamps L, Brücker C, Geyer TF (2017) Airfoil Self Noise Reduction at Low Reynolds Numbers Using a Passive Flexible Trailing Edge. 23rd AIAA/CEAS Aeroacoustics Conf (June):1–10, DOI 10.2514/6.2017-3496

Kunze S, Brücker C (2012) Control of vortex shedding on a circular cylinder using self-adaptive hairy-flaps. Comptes Rendus - Mec 340(1-2):41–56, DOI 10.1016/j.crme.2011. 11.009

Meyer KE, Cavar D, Pedersen JM (2007) POD as tool for comparison of PIV and LES data. 7th Int Symp Part Image Velocim pp 1–12

Osterberg N, Albertani R (2017) Investigation of self-deploying high-lift effectors applied to membrane wings. Aeronaut J 121(1239):660–679, DOI 10.1017/aer.2017.10

Perret L (2009) PIV investigation of the shear layer vortices in the near wake of a circular cylinder. Exp Fluids 47(4-5):789–800, DOI 10.1007/s00348-009-0665-y

Ponitz B, Schmitz A, Fischer D, Bleckmann H, Brücker C (2014) Diving-flight aerodynamics of a peregrine falcon (Falco peregrinus). PLoS One 9(2), DOI 10.1371/journal. pone.0086506

Prasad A, Williamson CHK (1997) The instability of the shear layer separating from a bluff body. J Fluid Mech 333:S0022112096004326, DOI 10.1017/ S0022112096004326

Rajagopalan S, Antonia RA (2005) Flow around a circular cylinder-structure of the near wake shear layer. Exp Fluids 38(4):393–402, DOI 10.1007/s00348-004-0913-0

Rodríguez I, Lehmkuhl O, Borrell R, Oliva A (2013) Direct numerical simulation of a NACA0012 in full stall. Int J Heat Fluid Flow 43:194–203, DOI 10.1016/j. ijheatfluidflow.2013.05.002

Rosti ME, Kamps L, Brücker C, Omidyeganeh M, Pinelli A (2017) The PELskin project-part V: towards the control of the flow around aerofoils at high angle of attack using a self-activated deployable flap. Meccanica 52(8):1811–1824, DOI 10.1007/s11012-016-0524-x

Schlüter JU (2010) Lift Enhancement at Low Reynolds Numbers Using Self-Activated Movable Flaps. J Aircr 47(1):348–351, DOI 10.2514/1.46425

Semeraro O, Bellani G, Lundell F (2012) Analysis of time-resolved PIV measurements of a confined turbulent jet using POD and Koopman modes. Exp Fluids 53(5):1203–1220, DOI 10.1007/s00348-012-1354-9

Stanek FJ (1965) Free and Forced Vibrations of Cantilever Beams With Viscous Damping. Tech. Rep. June, National Aeronautics and Space Administration, Washington DC

Tam CKW (1974) Discrete tones of isolated airfoils. J Acoust Soc Am 55(6):1173–1177, DOI 10.1121/1.1914682

Yarusevych S, Sullivan PE, Kawall JG (2009) On vortex shedding from an airfoil in low-Reynolds-number flows. J Fluid Mech 632:245, DOI 10.1017/S0022112009007058